Materials Today Bio 17 (2022) 100457

Contents lists available at ScienceDirect

Materials Today Bio

journal homepage: www.journals.elsevier.com/materials-today-bio

Induction of ferroptosis using functionalized iron-based nanoparticles for anti-cancer therapy

Chaewon Bae [a], Hyerim Kim [a], Yun-Min Kook [b], Chaedong Lee [c], Changheon Kim [a], Chungmo Yang [a], Min Hee Park [d], Yuanzhe Piao [c,e], Won-Gun Koh [f], Kangwon Lee [g,h,*]

[a] Program in Nanoscience and Technology, Graduate School of Convergence Science and Technology, Seoul National University, Seoul, 08826, Republic of Korea
[b] Center for Biomaterials, Biomedical Research Institute, Korea Institute of Science and Technology (KIST), Seoul, 02792, Republic of Korea
[c] Graduate School of Convergence Science and Technology, Seoul National University, 145 Gwanggyo-ro, Yeongtong-gu, Suwon-si, 16229, Republic of Korea
[d] THEDONEE, 1208, 156, Gwanggyo-ro, Yeongtong-gu, Suwon-si, Gyeonggi-do, 16506, Republic of Korea
[e] Advanced Institutes of Convergence Technology, Seoul National University, 145, Gwanggyo-ro, Yeongtong-gu, Suwon-si, Gyeonggi-do, Republic of Korea
[f] Department of Chemical and Biomolecular Engineering, Yonsei University, Seoul, 03722, Republic of Korea
[g] Department of Applied Bioengineering, Graduate School of Convergence Science and Technology, Seoul National University, Seoul, 08826, Republic of Korea
[h] Research Institute for Convergence Science, 145, Gwanggyo-ro, Yeongtong-gu, Suwon-si, Gyeonggi-do, Republic of Korea

ARTICLE INFO

Keywords:
Ferroptosis
Cancer nanomedicine
Biomaterials
Iron-based nanoparticles
Fenton reaction
Reactive oxygen species

ABSTRACT

Ferroptosis, a cell death pathway that is induced in response to iron, has recently attracted remarkable attention given its emerging therapeutic potential in cancer cells. The need for a promising modality to improve chemotherapy's efficacy through this pathway has been urgent in recent years, and this non-apoptotic cell death pathway accumulates reactive oxygen species (ROS) and is subsequently involved in lipid peroxidation. Here, we report cancer-targeting nanoparticles that possess highly efficient cancer-targeting ability and minimal systemic toxicity, thereby leading to ferroptosis. To overcome the limit of actual clinical application, which is the ultimate goal due to safety issues, we designed safe nanoparticles that can be applied clinically. Nanoparticles containing ferroptosis-dependent iron and FDA-approved hyaluronic acid (FHA NPs) are fabricated by controlling physicochemical properties, and the FHA NPs specifically induce ROS production and lipid peroxidation in cancer cells without affecting normal cells. The excellent *in vivo* anti-tumor therapeutic effect of FHA NPs was confirmed in the A549 tumor-bearing mice model, indicating that the induction of FHA NP-mediated cell death via the ferroptosis pathway could serve as a powerful platform in anticancer therapy. We believe that this newly proposed FHA NP-induced ferroptosis strategy is a promising system that offers the potential for efficient cancer treatment and provides insight into the safe design of nanomedicines for clinical applications.

1. Introduction

Nanomedicines are broadly advancing in cancer treatment, providing new expectations and opportunities to improve cancer treatment effectiveness. Nanoparticle research has been actively underway, and these agents can reduce side effects and provide accurate targeting without toxicity [1–4]. Nanoparticle-based chemotherapy for anticancer research has been meticulously designed with respect to its size, shape, composition, and targeting moiety. Still, nanoparticle-based chemotherapy remains difficult to apply clinically and remains an unresolved challenge [5,6]. Moreover, many studies have been conducted using optimally selected components to overcome the characteristics of tumors and target cells, but many problems remain [7–10]. Attached to increase the target effect, moieties reduce side effects. However, given that moieties are only effective for specific cancers, a more fundamental treatment is needed that involves the application of cancer cell death mechanisms to overcome these barriers.

The therapeutic means clinically applied and studied in cancer nanomedicine involve the death of cancer cells through apoptosis, necrosis, and necroptosis, which are traditionally known pathways. However, there are still some regrettable areas in clinical application [11–15]. Ferroptosis, a cell death pathway regulated by iron ions, was discovered in 2012 and has received attention over the past few years given its potential to eliminate tumor cells [16]. In this process, the Fenton

* Corresponding author. Department of Applied Bioengineering, Graduate School of Convergence Science and Technology, Seoul National University, Seoul, 08826, Republic of Korea.
E-mail addresses: orangechae@snu.ac.kr (C. Bae), kangwonlee@snu.ac.kr (K. Lee).

https://doi.org/10.1016/j.mtbio.2022.100457
Received 22 July 2022; Received in revised form 6 October 2022; Accepted 8 October 2022
Available online 14 October 2022

reaction between iron ions and intratumoral H_2O_2 induces reactive oxygen species (ROS), and interconversion occurs between its ferric (Fe^{3+}) and ferrous (Fe^{2+}) forms, eventually leading to lipid peroxidation of saturated fatty acids [17–19]. The mechanism of ferroptosis has not yet been fully elucidated, but in recent years, active research is being conducted on the possibility of ferroptosis as a new alternative to cancer nanomedicine [20–27].

Chemotherapy carriers that effectively deliver therapeutic particles and are biocompatible are very important for cancer therapy, among which hyaluronic acid (HA) is widely studied for cancer treatment given its superior properties. HA is a natural polysaccharide composed of repeat units of D-glucuronic acid and N-acetyl-D-glucosamine and can be chemically bound or modified by carboxyl and hydroxyl groups. Moreover, due to its non-immunogenicity, biocompatibility, biodegradability, and non-toxic, HA is widely used for biomedical applications and is easily degraded by hyaluronidase. HA is a ligand of the CD44 receptor overexpressed in cancer cells compared to normal cells and has the characteristics of providing tumor-selective targeting and internalization with HA binding and high affinity [28,29]. Based on these properties, HA-based carriers can improve the stable effects of anticancer therapy, and more efficient and satisfactory therapeutic effects can be achieved through harmless but improved targeting.

In this study, we designed HA-based nanoparticles with Fe (FHA NPs) to induce ferroptosis with high tumor-killing activity. Various cancer treatment strategies based on ferroptosis have been proposed, but limitations exist in actual clinical application, which is the ultimate goal due to the safety problem. So, FHA NPs are engineered to be safe nanoparticles for clinical applications with a physicochemically controlled, fine-tuned manufacturing process using FDA-approved materials. FHA NPs are not just a simple HA coating on iron but are constructed through natural coordination, ionic bonding, hydrogen bond, and electrostatic bonding without additional linkers and are manufactured through the formation of a pre-gel solution [30,31]. To construct safe and practically viable nanoparticles for clinical use, no specific dyes were added, and FDA-approved hyaluronic acid was used to provide biocompatibility, eliminating worries about toxicity or side effects. In addition, the fabricated FHA NPs can selectively target only cancer cells except for normal cells by using the properties of HA and can target a wide range of cancer cells without the use of commonly used targeting moieties (e.g., antibodies, small molecules, peptides). The effect was confirmed experimentally in various cancer cell lines. The FHA NP system, which induces ferroptosis in tumors, has been systematically proven to exhibit potent anticancer therapeutic effects and provides important insights and possibilities for potential chemotherapy regimens based on ferroptosis.

2. Materials and methods

2.1. Materials

Sodium hyaluronate ($M_W = 4.8 \times 10^3$ Da) of research-grade was purchased from Lifecore Biomedical (Chaska, MN, USA). Iron (II) chloride tetrahydrate ($FeCl_2{\cdot}4H_2O$) and ammonia solution (28 wt % in water) were purchased from Junsei Chemicals Co. (Tokyo, Japan). Iron (III) chloride hexahydrate ($FeCl_3{\cdot}6H_2O$, 97%) was purchased from Samchun Chemicals (Pyeongtaek, Korea). Dialysis membranes with a M_W cutoff of 3500 g/mol were purchased from Cellu-Sep®. Single donor human red blood cells were purchased from Innovative Research (Novi, MI). The Cell Counting Kit-8 (CCK-8) for viability assays was purchased from DoGen (EZ-Cytox, Korea). The Live/Dead Viability/Cytotoxicity Kit and the CellROX Orange Oxidative Stress Reagent were purchased from Invitrogen (Carlsbad, CA, USA). Prussian blue, Ferrostatin-1, α-tocopherol, and 4′,6-Diamidino-2-phenylindole (DAPI) were purchased from Sigma Aldrich (USA). Nuclear fast red, RSL3, and optimum cutting temperature (OCT) compound were purchased from TCI (Tokyo, Japan), Selleckchem (Houston, TX, USA), and Leica (UK), respectively. MitoTracker Deep Red FM, LysoTracker Deep Red, and BODIPY 581/591C11 were purchased from Invitrogen. FerroOrange was purchased from Dojindo. Hematoxylin and Eosin (H&E) staining kit was purchased from Abcam (ab245880, USA).

2.2. Preparation of iron/hyaluronic acid nanoparticles (FHA NPs)

Sodium hyaluronate (5 mg) was added to 50 mL of deionized water (DW) and then sufficiently stirred until the HA dissolved completely. Then, $FeCl_2{\cdot}4H_2O$ (99.4 mg) in DW (10 mL) was slowly added to the HA aqueous solution with stirring for 30 min. Then, $FeCl_3{\cdot}6H_2O$ (149.1 mg) in DW (10 mL) was slowly added to this solution. After 1 h under stirring, ammonia solution (1.5 M in DW) was added to adjust the solution's pH to basicity for coprecipitation. After stirring for 30 min, the product was separated using a strong magnet, washed several times, and then redispersed in 50 mL of 0.005 M HCl. The homogeneously and sufficiently dispersed NPs were further purified by dialysis (M_W cutoff 3.5 K) for 24 h and stored at −4 °C.

2.3. Characterization of FHA NPs

The dynamic light scattering (DLS), ζ-potential, and polydispersity index (PDI) of the NPs were confirmed by a zetasizer Nano ZS (Malvern Instruments, UK). The UV–visible absorption spectrum of FHA NPs was analyzed using a microplate reader (Synergy H1, Hybrid reader, USA). Field emission scanning electron microscopy (FE-SEM) (JSM-7800 F Prime, JEOL Ltd., Japan) and energy filtering transmission electron microscopy (TEM) (LIBRA 120, Carl Zeiss, Germany) operated with an acceleration voltage of 120 kV were used to confirm the surface topography and morphology of the FHA NPs. The amount of iron in FHA NPs was quantified by inductively coupled plasma-atomic emission spectroscopy (ICP-AES) (Optima 8300; Perkin-Elmer, USA).

2.4. Hemolysis assay

Human red blood cells were diluted with phosphate-buffered saline (PBS), and the diluted blood was dispensed into 1.5 mL microfuge tubes. Each concentration of FHA NPs was added to each blood and incubated for 2 h. And then centrifuged at 500 g for 10 min. PBS was used as negative controls (0% lysis), and triton X-100 was used as positive controls (100% lysis). The absorbance at 540 nm was confirmed (Microplate reader, Bio Tek H1, USA) and the percent hemolysis was calculated using the following formula. Hemolysis (%) = $(A_{\text{FNA NPs}} - A_{\text{negative control}})/(A_{\text{positive control}} - A_{\text{negative control}}) \times 100$.

2.5. Cell culture

Human fibroblasts (HFBs), human breast adenocarcinoma cells (MCF7), human colon carcinoma cells (HCT116), and human lung carcinoma cells (A549) were purchased from Koran Cell Line Bank (Seoul, Korea). HFBs were maintained in Dulbecco's modified Eagle medium (DMEM), all cancer cells were controlled in RPMI 1640 (Welgene, Korea), consisting of 10% fetal bovine serum (FBS) (Cellsera, NSW, Australia) and 1% penicillin/streptomycin (Welgene, Korea). And each cell line was cultured in a suitable environment of 5% CO_2 and 37 °C.

2.6. Cell viability

Each cell was seeded into a 96-well plate and stabilized overnight and washed. Each well was treated with suspensions at different concentrations of FHA NP (6.25, 12.5, 25, 50, 100, and 200 μg/mL) in medium and then incubated for 1, 3, 6, and 12 h at 37 °C. Cell viability was analyzed by WST assay using EZ-Cytox (DoGen, Korea). After the addition of 10 μL of EZ-Cytox solution to each well, incubated for 3 h, and a wavelength of 450 nm was measured.

2.7. Fluorescence-activated cell sorting (FACS)

After detaching each cell, 1×10^6 cells were prepared as a sample in a volume of 100 μl. FITC Mouse Anti-Human CD44 (BD Biosciences) was used as the antibody. After adding the antibody, each sample was incubated at 4 °C for 30 min. Following the wash 3 times by centrifugation at 400*g*, the cells are resuspended in ice-cold PBS. Then, 10,000 events of cells were analyzed using a Guava EasyCyte flow cytometer (Millipore, Boston, USA).

2.8. Live/dead assay

After seeding 5×10^4 cells, various concentrations of FHA NPs were treated in the medium for 12 h. After washing with DPBS to remove residual FHA NPs, 2 μM Calcein AM and 4 μM ethidium homodimer-1 (EthD-1) were applied 30 min before fluorescence imaging at room temperature. And then we confirmed it through a laser scanning microscope (Carl Zeiss, Oberkochen, Germany).

2.9. Reactive oxygen species (ROS) analysis

CellROX Orange Oxidative Stress Reagent (Invitrogen, Carlsbad, CA, USA) was used to confirm intracellular ROS expression. Briefly, 5×10^4 cells were seeded and then cultured overnight. Different concentrations of FHA NPs (6.25, 12.5, 25, 50, 100, and 200 μg/mL) in the fresh medium were then added for an additional 12 h. After three washes with DPBS, the CellROX Orange Oxidative Stress Reagent was directly added to 300 μL at a final concentration of 5 μmol/L. After 30 min, DAPI was added for 5 min to counterstain the nuclei. To confirm the qualitative evaluation of intracellular ROS distribution, the labeled cells were confirmed using a laser scanning microscope. For quantification of fluorescence, each labeled cell was analyzed with a Guava EasyCyte flow cytometer.

2.10. Prussian blue staining

After seeding 5×10^4 cells, the cells were treated with FHA NPs for 12 h. Then, the cells were stained with a mixture of 5 wt% Prussian blue ($C_6Fe_2KN_6 \bullet xH_2O$) (Sigma Aldrich, USA) and 10% HCl (1:1), washed three times, and the cells were counterstained using nuclear fast red (TCI, Tokyo, Japan). After washing, the cells were dehydrated sequentially with 10%, 90%, and 100% alcohol and then cleared in xylene for 3 min. The cells were coverslipped using a permanent aqueous mounting medium (Dako, USA) for microscopic study.

2.11. Tomography images

A549 cells were plated on TomoDish and treated with FHA NPs at a concentration of 200 μg/mL for 12 h and then washed three times. Control cells not treated with FHA NPs were also prepared in the same manner. DAPI was added for 5 min to stain the nucleus and commercial ODT (HT-1H; Tomocube Inc., Korea) that can be confirmed with a high refractive index (RI) value to distinguish 3D intracellular locations was used.

2.12. Real-time reverse transcriptase-polymerase chain reaction (real-time RT-PCR)

Total RNA was isolated by the TRIzol method (Life Technologies, CA, USA), and cDNA was synthesized using a cDNA Synthesis Kit (Maxime RT PreMix, Intron, Korea). The cDNA was amplified by real-time RT-PCR with RealMOD Green SF 2X qPCR mix (iNtRon Biotechnology, Korea) using the QuantStudio5 Real-Time PCR system (Applied Biosystems, USA) with the following parameters: Proceed with initial activation to denaturation 10 min at 95 °C and denature for 15 s at 95 °C. And after annealing at 60 °C for 30 s, finally, proceed to the extension step of 5 min at 72 °C. The primer sequences were as follows: BAX, 5′-AGGCGGCGGGCCCACCAGCTC-3′ (sense) and 5′-CATCAGCAAA-CATGTCAGCTG-3′ (antisense); Ripk1, 5′-GGCATTGAA-GAAAAATTTAGGC-3′ (sense) and 5′-TCACAACTGCATTTTCGTTTG-3′ (antisense); GPX4, 5′-ACAAGAACGGCTGCGTGGTGAA-3′ (sense) and 5′-GCCACACACTTGTGGAGCTAGA-3′ (antisense); and β-Actin, 5′-GTGGGCCGCTCTAGGCACCAA-3′ (sense) and 5′- CTCTTTGATGTCACG-CAGGATTTC -3′ (antisense). The quantity of mRNA was normalized by the expression of β-Actin.

2.13. Western blot

After preparing MCF7, HCT116, and A549 cells treated with or without FHA NP, each cell was washed and lysed in RIPA buffer with Xpert phosphatase inhibitor cocktail solution (GenDEPOT). Proteins were then separated by 12% SDS-PAGE, transferred to membranes, blocked with 5% skim milk, incubated with primary antibodies: β-Actin (1:1000, 4970, Cell Signaling, USA), BAX (1:1000, ab32503, Abcam, UK), RIPK1 (1:1000, 3493, Cell Signaling, USA), GPX4 (1:1000, ab125066, Abcam, UK) and subsequently treated secondary antibody (1:3000, ab6721, Abcam, UK). The bands on PVDF were detected with a Las 4000 device (Fujifilm Life Science, USA) using Clarity Western ECL substrate (Bio-Rad).

2.14. Inhibition assay

Cells were prepared under the same conditions described above in 5. Cell viability. FHA NPs were added to each well with Ferrostatin-1 (Sigma Aldrich, USA), RSL3 (Selleckchem, Houston, TX, USA), and α-tocopherol (vitamin E) (Sigma Aldrich, USA). EZ-Cytox was performed after 12 h.

2.15. Staining of mitochondria and lysosome

Intracellular mitochondria and lysosomes were identified using MitoTracker Deep Red FM (Invitrogen) and LysoTracker Deep Red (Invitrogen). Using A549 cell lines, the group was divided into an FHA NPs treated group and a non-treated group, and MitoTracker and LysoTracker were added at a final concentration of 100 nM and 50 nM after 12 h of treatment with 200 μg/mL concentration of FHA NPs, respectively. After 30 min of treatment, the labeled cells were confirmed using a laser scanning microscope after counterstaining with DAPI and Alexa 488 Phalloidin.

2.16. Staining of FerroOrange

Using A549 cell lines, the group was divided into an FHA NPs treated group and a non-treated group, and FHA NPs were treated at a concentration of 200 μg/mL for 24 h, and then FerroOrange and LysoTracker were treated with 1 μM and 50 nM concentrations, respectively. After 30 min of treatment, the labeled cells were confirmed using a laser scanning microscope after counterstaining with DAPI.

2.17. Animal models and tumor inoculation

Four-to five-week-old male athymic Balb/c Nude mice (17 ± 1 g) were supplied by Dooyeol Biotech, Inc. (Seoul, Korea). The mice were maintained at 25 ± 1 °C with adequate water and food (Woojungbio, Co., LTD., Suwon, Korea) (IACUC Permit Number: WJIACUC20180911-3-28). To develop the tumor model, A549 cells (2.5×10^6 cells per 100 μL) were subcutaneously injected into the left and right legs of each mouse. Average initial tumor volumes of 330 mm^3 were used for all studies. For *in vivo* studies, A549 tumor-bearing mice have separated into seven groups and the number of mice per group was three. The mice were administered FHA NPs (8 mg/kg) every 24 h by peritumoral subcutaneous injection. Control mice were compared by injecting the same volume of PBS together. Tumor growth was confirmed by measuring the

vertical diameter, and the tumor volume was calculated with the following equation:

2.18. Ex vivo MRI

FHA NP accumulation was monitored in the whole tumor and organs (heart, spleen, liver, kidney, and lung) by ex vivo MRI. The MRI experiments were performed on a Bruker Biospec 7 T system (BioSpec 70/20 USR; Bruker, Germany) using a 35 mm quadrature volume coil. The scanning parameters were TR = 200 ms, TE = 10 ms, and a 1 mm average slice thickness.

2.19. Histological analysis

Tumors obtained from the sacrificed mice were fixed with 3.7% formaldehyde (Dana Korea, Korea) for 12 h and saturated with 30% sucrose in PBS. For histology, frozen tumors were embedded in OCT and stored at −80 °C. Then, 10 μm thick cryo-sections were stained with H&E and observed.

2.20. Statistical analysis

Statistical significance was evaluated using one-way ANOVA with Tukey's test. When the P-value was less than 0.05, the difference was considered statistically significant. (marked as *).

3. Results and discussion

3.1. Preparation and characterizations of engineered FHA NPs

In this work, we report an effective and accurate tumor-targeting system via the FHA NP-mediated ferroptosis pathway (Fig. 1). The interaction between HA and receptors CD44 triggers receptor-mediated endocytosis and sequentially induces intracellular delivery and responses [32–35]. FHA NP is decomposed by endogenous hyaluronidase (HAase) in lysosomes after endocytosis, where Fe is released, a Fenton reaction, ROS induction proceeds sequentially, and finally leads to cell death by lipid peroxidation. HA was adopted as a surface binding ligand given its inherent ability to target CD44 receptors to confer biocompatibility, biodegradable, and natural polymers. Briefly, the negatively charged carboxyl groups (COO^-) of HA interact with Fe^{2+}/Fe^{3+} ions to form a chain strengthened by coordination bonding based on a modified pre-gel method. The size distribution of FHA NPs, which was determined by dynamic light scattering (DLS), was plotted (Fig. S1) as a function of the concentration of HA at 0.005, 0.01, 0.05, 0.5 wt%. In the case of the concentration of HA was 0.01 wt%, the average diameter of FHA NPs under 0.005 M HCl storage condition is about 102 ± 5 nm, and based on these results, all experiments were performed with FHA NPs formed with 0.01 HA wt%. We confirmed FHA NP formation based on the differences in UV–Vis spectra between HA NPs containing Fe and multiple control groups (HA only, $FeCl_2$ only, and $FeCl_3$ only) (Fig. 2A) and comparisons of the X-ray diffraction (XRD) patterns of HA polymer, iron oxide, and FHA NPs (Fig. S2). Fig. 2B shows similar characteristic peaks of Fe oxide NPs at 2θ = 30.3°, 35.8°, 43.5°, 53.9°, 57.3°, and 62.8°, respectively, and we were confirmed that the FHA NPs obtained by coprecipitation contained some form similar to Fe_3O_4 in addition to iron bound to HA [36]. The particle size and shapes were confirmed by SEM (Fig. 2C) and TEM (Fig. 2D, S3), and the energy dispersive X-ray spectroscopy (EDS) data of FHA NP are shown in Fig. S4. The actual amount of internalized Fe in the FHA NPs was determined by ICP-OES to quantify the amount of Fe as a function of the concentration of FHA NPs for the subsequent *in vitro* assay (Fig. 2E). As the concentration of FHA NPs increased, the loading efficiency increased linearly with increasing iron ion concentrations (R^2 = 0.9971). The measured zeta potential was 30 ± 1.9 mV at pH 4, 16 ± 0.7 mV at pH 7, and -8±1.2 mV at pH 10, due to the carboxylic groups. The zeta potential was significantly enhanced at Ph 4 due to the protonation of the carboxyl group in HA. As shown in Fig. S5, the measured average size of the FHA NPs at pH 7 was approximately 400 nm, revealing

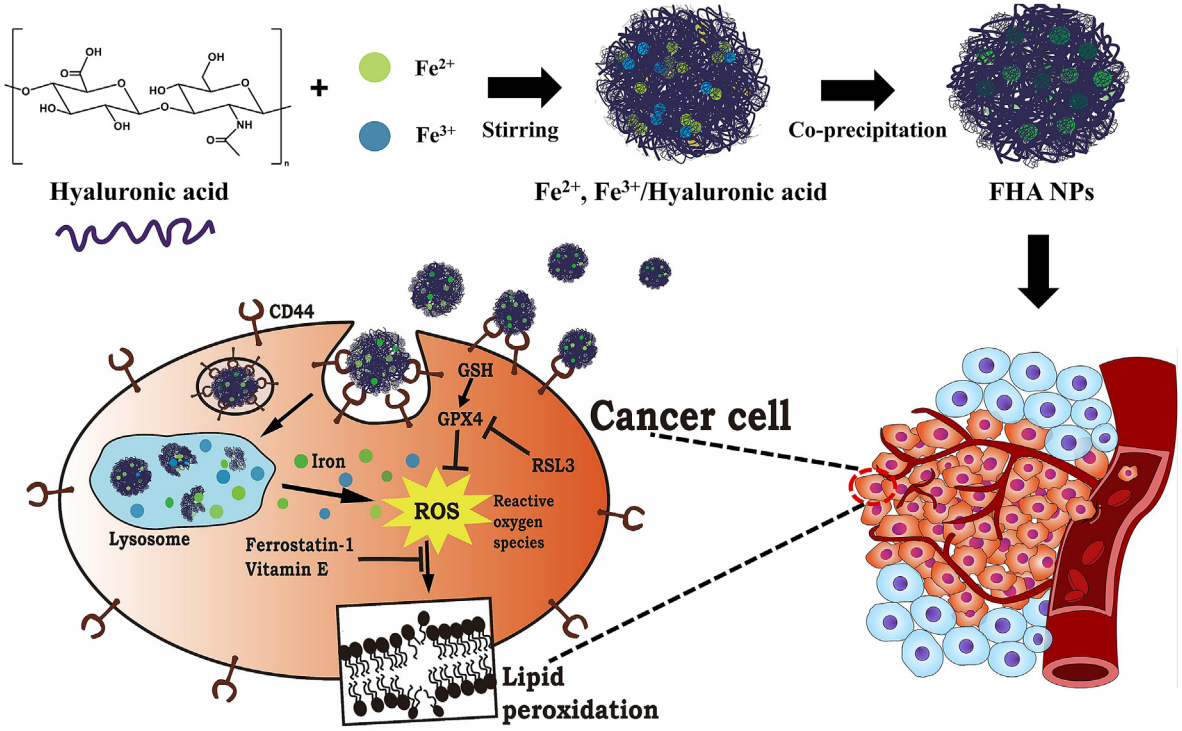

Fig. 1. Schematic representation of the induction of ferroptosis by FHA NPs as an anticancer therapeutic. Schematic illustration of the strategy for the construction of FHA NPs and the sequential events of FHA NPs mediated by iron and HA: tumor-specific binding, cellular internalization, FHA NPs degradation and iron release, ROS generation, and lipid peroxidation.

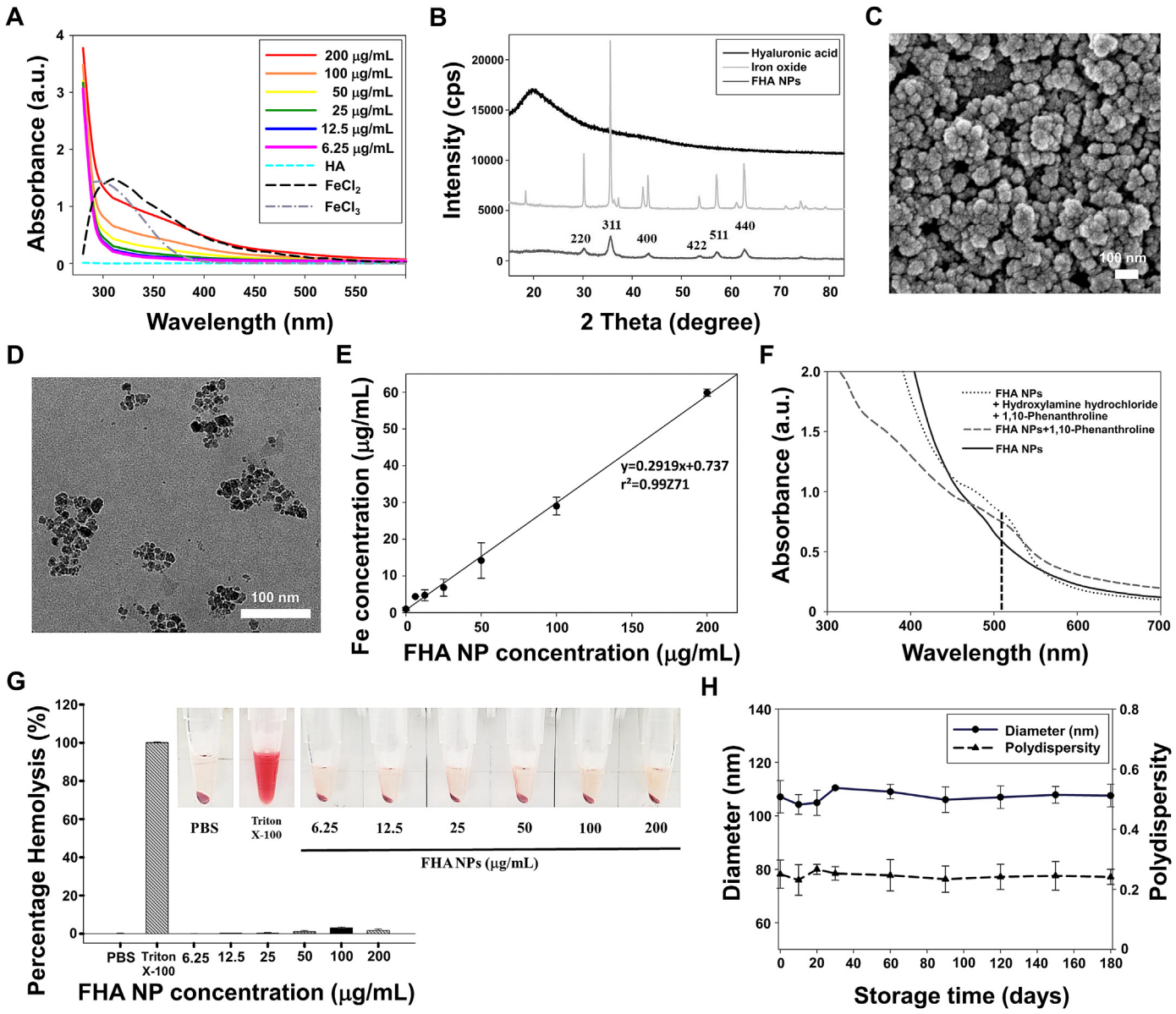

Fig. 2. Characterization of FHA NPs. (A) Comparison of the UV–visible spectrum of HA, $FeCl_2$, $FeCl_3$, and different concentrations of FHA NPs. The absorbance spectra were measured using a UV–visible spectrophotometer. (B) X-ray diffraction patterns of (C) SEM images of FHA NPs. (D) TEM images of FHA NPs. (E) Quantification of iron (Fe) in internalized NPs measured using ICP-OES. (F) The absorption spectrum of FHA NPs, FHA NPs treated with 1,10-phenanthroline, and FHA NPs treated with hydroxylamine hydrochloride and 1,10-phenanthroline. (G) Relative comparison and photograph of hemolytic activity according to different concentrations of FHA NPs. (H) Stability of FHA NPs based on the size and polydispersity index (PDI) over a six-month period. The graph presents the change in particle size and PDI under storage conditions.

agglomeration compared to the size distribution at pH 4. The distribution change tendency at pH 10 exhibited a broad diameter distribution than the size distribution change compared to that at pH 4. Based on these data, the stability of the FHA NPs was evaluated in 0.005 M HCl and deionized water (DW), separately. In addition, the iron ions contained in FHA NPs were confirmed through 1,10-phenanthroline and hydroxylamine hydrochloride after treated hyaluronidase (Fig. 2F). 1,10-phenanthroline forms a lupus complex with Fe^{2+}, enabling quantitative analysis of Fe^{2+}. And iron existing in the Fe^{3+} oxidation state was reduced to the Fe^{2+} oxidation state with hydroxylamine hydrochloride and confirmed using 1,10-phenanthroline. The absorption spectrum of iron (III) chloride and iron (III) chloride were confirmed in the absence and presence of 1, 10-phenanthroline and hydroxylamine hydrochloride (Figs. S6, S7, S8, S9, S10). In the same way, the absorption spectrum of FHA NPs was confirmed in the absence and presence of 1,10-phenanthroline and hydroxylamine hydrochloride, and the presence and ratio of Fe^{2+} and Fe^{3+} were confirmed through the difference in absorbance around 510 nm. The absorbance intensity of 510 nm was 0.584 for FHA NPs, 0.745 for FHA NP treated with 1,10-phenanthroline, and 0.823 for FHA NP treated with hydroxylamine hydrochloride and 1,10-phenanthroline. Through these results, the presence of ionic iron through the binding of HA and iron ions in FHA nanoparticles was confirmed, and the ratio of Fe^{2+}: Fe^{3+} was 2.06: 1.

To validate the biocompatibility of FHA NPs in this study, hemolysis tests were performed on human blood. The hemolytic properties were confirmed at each concentration of 6.25, 12.5, 25, 50, 100, and 200 μg/mL FHA NPs, and PBS and triton X-100 were used as negative and positive controls, respectively (Fig. 2G, S11). As a result of incubating blood with FHA NPs for 2 h, hemolysis rates of less than 2% were confirmed at all concentrations of FHA NPs. Considering the critical safe hemolysis

rate of the biomaterial, less than 5% was considered non-hemolytic, and based on this, we confirmed that the FHA NPs we developed were biocompatible. As shown in Fig. S12, the difference between storage conditions in DW (i) and in 0.005 M HCl (ii) was also observed with the naked eye, which confirmed that FHA NP was well dispersed based on the pH of the acidic aqueous phase. FHA NPs were more stable in 0.005 M HCl compared to DW, and no additional precipitation or significant changes in size (105 ± 2 nm) and PDI (0.24 ± 0.01) of the FHA NPs were observed for six months, demonstrating excellent physicochemical stability (Fig. 2H).

3.2. Cellular uptake of FHA NP and induction of death by ferroptosis

To confirm the effect on cell viability, various concentrations of FHA NPs from 6.25 μg/mL to 200 μg/mL were treated for 1, 3, 6, and 12 h and then analyzed with CCK-8. The *in vitro* capability of FHA NPs was confirmed using human breast adenocarcinoma cells (MCF7) (Fig. 3B), human colon carcinoma cells (HCT116) (Fig. 3C), and human lung carcinoma cells (A549) (Fig. 3D) compared to the control cells (human fibroblast cells (HFBs)) (Fig. 3A). Compared with the FHA NP-free control, only 32.7 ± 5%, 13.7 ± 5%, and 23.6 ± 1% of MCF7, HCT116, and A549 cells, respectively, survived after 12 h of 200 μg/mL FHA NP treatment. In normal cells, neither increasing the concentration of FHA NPs nor increasing the uptake time affected cell survival. In MCF7, HCT116, and A549 cells, the higher the concentration and the longer the treatment time, the more cancer cell death. Cell death was observed to be significantly induced exclusively in cancer cells compared to HFBs, even at a low concentration of 6.25 μg/mL FHA NPs. Also, after treatment with FHA NPs for 1, 3, 6, and 12 h, the viability of cancer cells was significantly reduced compared with normal cells. Next, CD44 expression was measured in HFB, MCF7, HCT116, and A549 cells, respectively. The expression of CD44 receptor expressed on the cell surface is a part closely connected to confirm the effectiveness of FHA NPs composed of HA. We performed FACS analysis to confirm the difference in the expression of CD44 in normal and cancer cells and the level of CD44 expression in each cancer cell. As shown in Fig. 3E, CD44 expression was detected in cancer cell lines but hardly detected in HFB cells. Furthermore, A549, HCT116, and MCF7 showed high expression in the order.

We then performed Live/Dead assays to visually confirm the cytotoxicity and cancer cell death effects of FHA NPs. As shown in Fig. 3F and S13, live-dead images of HFB, MCF7, HCT116, and A549 cells were obtained 12 h after incubation with an elevated dose (6.25–200 μg/mL) of FHA NPs (scale bar: 100 μm). The green color and red color indicate living and dead cells, respectively. As the concentration of NP increased from 6.25 to 200 μ/mL, we confirmed that the dead cell ratio of MCF7, HCT116, and A549 cells gradually increased and the ratio of living cells decreased. In contrast, most of the HFB cells were alive. These results demonstrate that cancer cell death increased with the concentration of FHA NPs, which was consistent with the tendency of viability as noted based on CCK-8 assays.

Studies on the relationship between ROS generation and cancer treatment are being actively conducted, and according to a number of reports, ROS plays a key role in cell death due to ferroptosis [36,37]. To observe oxidative stress levels, we stained the nuclei with DAPI and observed the expression of ROS, the accumulation of which occurs by the Fenton reaction, representing a key component in the molecular mechanisms of ferroptosis [38–40]. In Fig. 3G and S14, the presence of ROS at different FHA NP concentrations was confirmed using a laser scanning microscope. Here, blue represents the nucleus, and red represents the ROS (scale bar: 50 μm). As the concentration of FHA NPs increased, higher expression of ROS, a key factor of ferroptosis, was detected. We quantified ROS expression by FACS and plotted the fluorescence intensity (Fig. S15). Comparing the uptake of FHA NPs by HFB cells as well as MCF7, HCT116, and A549 cells for 12 h yielded results similar to those observed with the microscope. The mean fluorescence intensity relative to the concentration was the highest in A549 cells. Overall, in HFB cells, ROS expression did not exhibit any increase in fluorescence intensity with increasing FHA NP concentration; however, the fluorescence intensity increased with increasing FHA NP concentration in MCF7, HCT116, and A549 cells (Fig. 3H). These results showed that FHA NPs successfully induced cancer cell death without affecting normal cells. Although the cell death rate and the concentration of the affected FHA NPs differed depending on the characteristics of each cancer cell, the tendency of cancer cells to die based on the effects of the FHA NPs was the same. The Fenton reaction induces ROS. As more ROS are generated, more oxidative stress is induced. The remarkable performance of our designed FHA NPs in inducing ferroptosis demonstrated its promising ability to deliver Fe and trigger the Fenton response, increasing oxidative stress and promoting cancer cell death.

3.3. Labeling and identification of the in vitro cellular uptake of FHA NPs

Quantitative assessment of the cellular uptake of FHA NP is essential to confirm the absorbed amount of Fe in cells. The Prussian blue assay is widely used to measure cellular Fe content, relying on the reaction of Fe ions in a cell [41,42]. We performed qualitative and quantitative evaluations together to confirm the amount of cellular uptake. First, to evaluate the visual difference in cellular uptake of FHA NPs, we stained cells with Prussian blue after treatment with different concentrations of FHA NPs (Fig. 4A). Internalization of the FHA NPs was obviously increased in MCF7, HCT116, and A549 cells based on the increasing concentration of FHA NPs compared to HFB cells. Due to the effect of FHA NPs, an increase in the amount of Fe accumulated in the cells and lipid peroxidation leading to ferroptotic cell death were confirmed in microscopic images, and cell morphology was more severely altered as the concentration of FHA NPs increased. In addition, 3D refractive index (RI) tomography was performed in A549 cells after treatment without (Fig. 4B) and with (Fig. 4C) FHA NPs for 12 h using ODT. The RI values of the cells were indicated in yellow, the RI values of the FHA NPs were presented in red, and the nuclei were stained with DAPI (blue). When comparing the group not treated with FHA NPs and the group treated, we were confirmed that the cell morphology was very different (Fig. S16). Morphological changes similar to lipid peroxidation were confirmed without any abnormality in the nucleus, and the distribution of intracellular FHA NPs was high on the cell surface.

Quantification of cellular iron uptake according to FHA NP concentration was performed with ICP-OES measurements. Fig. 4D, E, 4F, and 4G shows the quantification of intracellular Fe concentration after FHA NP treatment and indicate the cellular uptake ratio. The amount of iron internalized within the cells was different for each cell line, and the amount of iron uptake at the same concentration of FHA NPs was also different. Cells were treated with 6.25–200 μg/mL FHA NPs, separately, to confirm the intracellular iron content. In FHB cells, the basic amount of iron present was 17.5 μg/mL. After exposure to FHA NPs, the average cellular iron content increased to 18.4 ± 2.8, 22.7 ± 2.5, 23.3 ± 3.7, 24.7 ± 4, 30.4 ± 1, and 36.4 ± 6 μg/mL, respectively (Fig. 4D). The amount of iron present in MCF7 cells was 8.8 ± 0.9 μg/mL at baseline. The intracellular iron content increased to 8.9 ± 0.2, 15.4 ± 0.2, 26.8 ± 2.8, 44.6 ± 3.5, 64.9 ± 0.5, and 66.4 ± 1.8 μg/mL, respectively (Fig. 4E). The amount of iron in HCT116 cells was 6.5 ± 0.5 μg/mL at baseline, and the iron levels increased to 13.9 ± 0.3, 15 ± 4.1, 25.3 ± 1.4, 31.6 ± 1.1, 38 ± 3.5, and 41.3 ± 0.3 μg/mL, respectively (Fig. 4F). The amount of iron present in A549 cells was 6.3 ± 2 μg/mL at baseline, and the iron content increased to 13.2 ± 1.8, 13.8 ± 2.7, 16.9 ± 4.5, 21.6 ± 5.2, 46.1 ± 2.3, and 47.9 ± 3.4 μg/mL, respectively (Fig. 4G).

The iron uptake results in the cells indicated that these FHA NPs successfully entered the cells at considerable levels. Treatment with higher concentrations of FHA NPs, iron uptake in MCF7, HCT116, and A549 cells was significantly increased compared with HFB cells. The ratios of Fe uptaken by the cells were calculated between the theoretical value of the cell and the absolute value uptake per cell versus the concentration of FHA NPs. The uptake ratio after exposure to 200 μg/mL

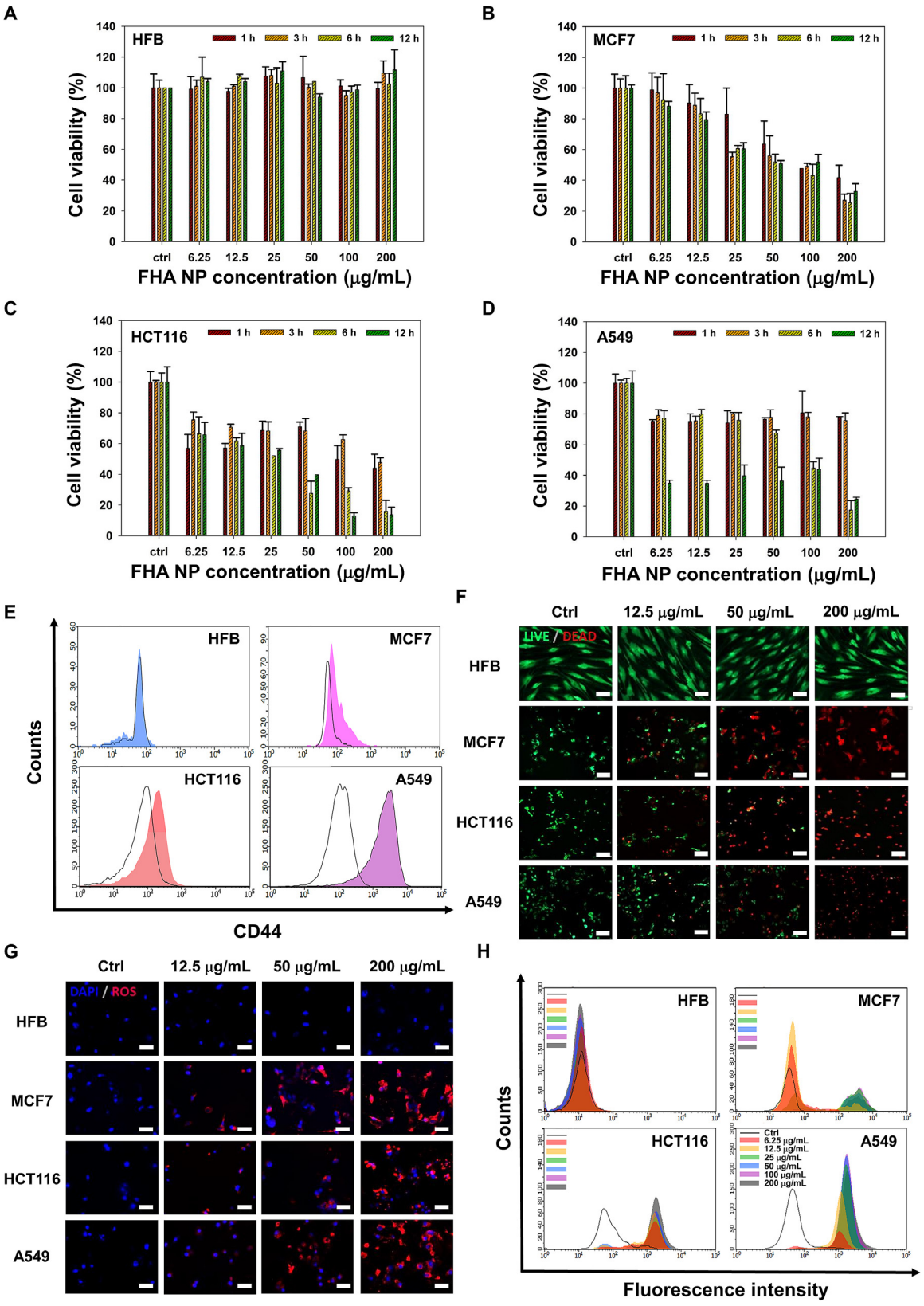

Fig. 3. Verification of viability and ROS generation in HFB, MCF7, HCT116, and A549 cells after treatment with FHA NPs. Viability in (A) HFB cells, (B) MCF7, (C) HCT116, and (D) A549 cancer cells after incubation with various concentration of FHA NPs for 1, 3, 6, and 12 h, separately, as determined using CCK-8 assays. (n = 5) The value is indicated as mean ± SD. (E) Flow cytometry analysis for CD44 expression in HFB, MCF7, HCT116, and A549 cells. Line, isotype control; color, CD44 expression. (F) Live/Dead assay in HFB, MCF7, HCT116, and A549 cells incubated with FHA NPs for 12 h as visualized with fluorescence microscopy. The green color and red color indicate living and dead cells, respectively. (scale bar: 100 μm) (G) Fluorescent images of CellROX Orange, representing ROS production. Blue and red indicate nuclear and ROS expression, respectively. (scale bar: 50 μm) (H) Flow cytometric analysis of intracellular ROS induction in cancer cell lines. Flow cytometric analysis was performed 12 h after treatment with various concentrations of FHA NPs.

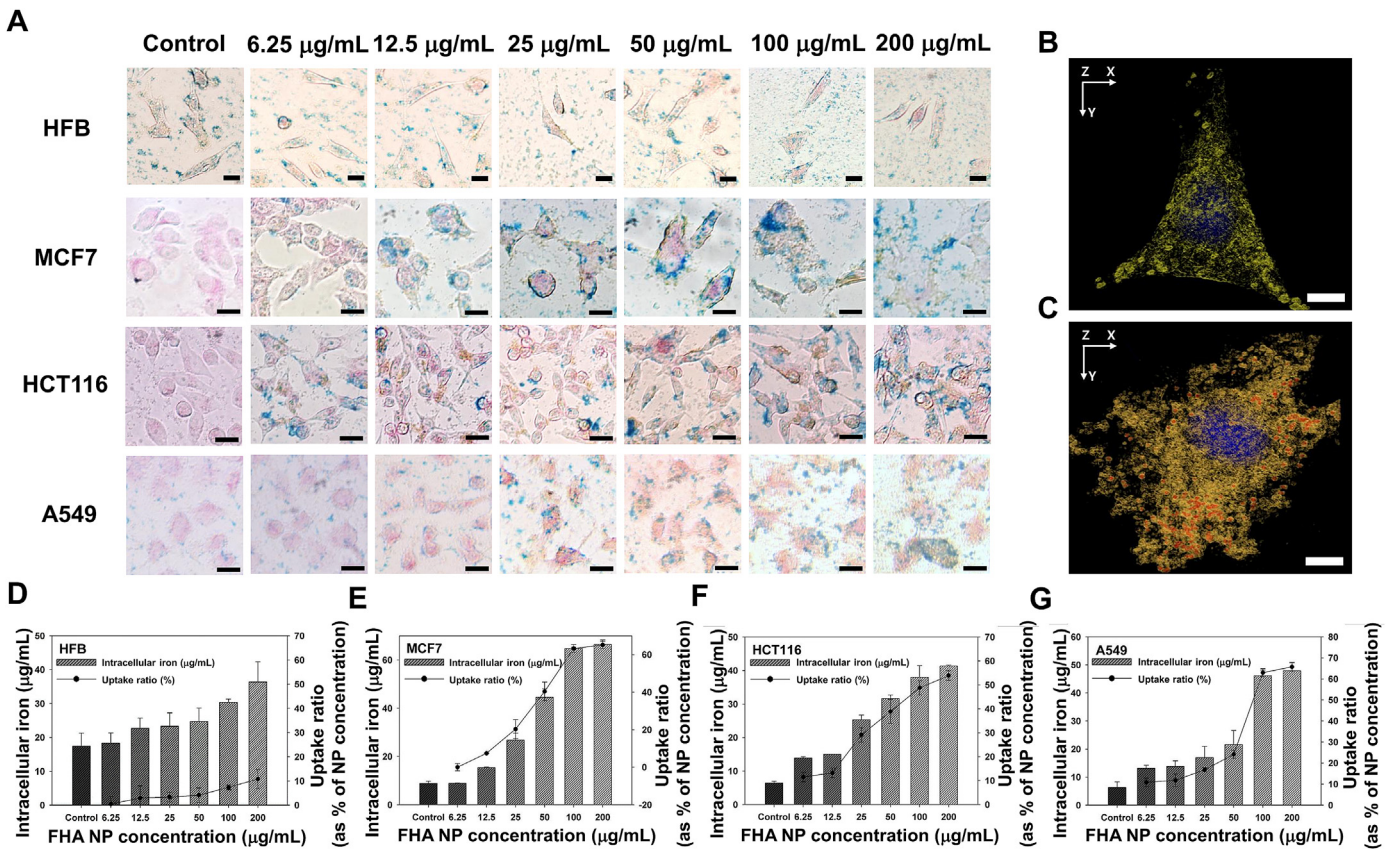

Fig. 4. Qualitative and quantitative confirmation of intracellular Fe content. (A) Microscopic images of MCF7, HCT116, and A549 cells incubated with different concentrations of FHA NP and stained with Prussian blue and red counterstain. The cytoplasm is light pink, and the nucleus is dark pink. Iron particles are depicted as blue dots. (scale bar: 20 μm) 3D tomography image of A549 cells (B)without and (C)with FHA NPs treatment confirmed through refractive index (RI) values. Yellow and red dots represent refractive index (RI) values of the cell and FHA NPs, and blue represents DAPI staining, respectively. (scale bar: 5 μm) Quantification of internalized FHA NPs in (D) HFB, (E) MCF7, (F) HCT116, and (G) A549 cells based on ICP-AES and uptake ratio concentration.

FHA NPs in MCF7, HCT116, and A549 cells differed (65.1 ± 2.3%, 53.9 ± 2.1%, and 65.7 ± 1.9%, respectively) compared with HFB cells (10.8 ± 3.7%). The sensitivity of internalization varies from cell line to cell line, but the mechanisms of these differences remain unknown. However, the differences in the regulation of iron uptake between normal cells and cancer cells may also partially explain the different internalization efficiencies reported here [17,43].

3.4. Identification of the underlying mechanisms of FHA NPs-induced cell death via ferroptosis

The diagram in Fig. 5A schematically illustrates the mechanism of ferroptosis cell death through down-regulation by FHA NP. To confirm the mechanism of FHA NP-induced lipid peroxidation through ferroptosis, we first performed real-time RT-PCR to analyze the mRNA levels in MCF7, HCT116, and A549 cells exposed to 200 μg/mL FHA NPs for 12 h. The mRNA levels of the following genes were confirmed: BAX, a key determinant of apoptosis expression; RIPK1, which is involved in the development of necrosis; and GPX4, a key factor known as a negative regulator of ferroptosis [44–47]. Comparison of the relative mRNA expression levels revealed a significant difference between BAX (Fig. 5B), RIPK1 (Fig. 5C), and GPX4 (Fig. 5D) in MCF7, HCT116, and A549 cells. The mRNA expression levels of the apoptotic gene BAX and necrotic gene RIPK1 did not significantly different compared to the group not treated with FHA NP, whereas the mRNA expression level of the ferroptotic gene GPX4 was significantly down-regulated in each cell line. FHA NPs exhibited a greater influence on GPX4 mRNA expression compared with BAX and RIPK1 mRNA expression; therefore, these results suggested that cell death-inducing FHA NPs are involved in the regulation of ferroptosis compared with apoptosis and necrosis. Furthermore, compared with the control group, RIPK expression was not significantly different, whereas BAX expression was slightly up-regulated, confirming that ferroptosis has an effect on apoptosis. Moreover, the association between ferroptosis and apoptosis has been previously reported [21]. These results suggest that FHA NPs represent a promising platform for cancer therapy by inducing ferroptosis, but further studies on the relationship between ferroptosis and apoptosis are needed. Next, differences in protein expression were identified by Western blot analysis (Fig. 5E). The expression level of each protein was confirmed using the primary antibody against β-Actin, BAX, RIPK1, and GPX4, identical to the mRNA gene confirmed by RT-PCR. Protein expression levels were confirmed in MCF7, HCT116, and A549 cells treated without and with 200 μg/mL FHA NPs, and a protein expression tendency similar to the mRNA expression level was confirmed. These results suggest that FHA NPs exposure induces cell death through ferroptosis through iron accumulation, rather than apoptosis or necrosis.

Next, the association between cell death and ferroptosis in HFB, MCF7, HCT116, and A549 cells was confirmed through RSL3, Ferrostatin-1, and tocopherol, which is known as vitamin E [16,44,48]. First, 200 μg/mL of FHA NPs and different concentrations of Ferrostatin-1, vitamin E, and RSL3 were used to treat A549 cells for 12 h, separately. Then, 4 μg/mL Ferrostatin-1, 100 μg/mL vitamin E, and 1 μg/mL RSL3 were selected as treatment concentrations based on equal effects (Fig. S17). The red dot in the upper left indicates cell viability without FHA NPs treatment. After treatment with FHA NP, greater than 70% cell death was noted. Based on the determined treatment concentrations, HFB cells (Fig. 5F), MCF7 cells (Fig. 5G), HCT116 cells (Fig. 5H), and A549 cells (Fig. 5I) were treated with RSL3 in the presence and

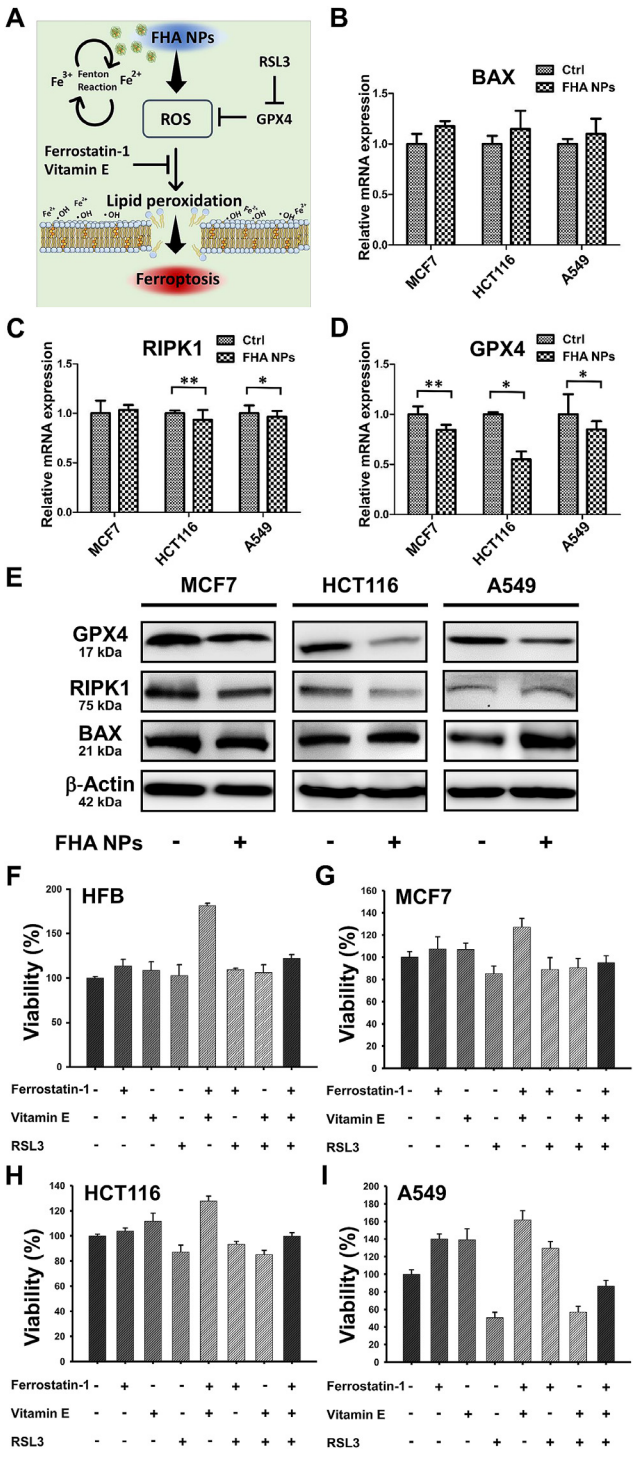

Fig. 5. Real-time RT-PCR analysis and verification of the inhibitory effect. (A) Schematic diagram of cell death mechanism of ferroptosis through down-regulation of FHA NP. Real-time RT-PCR analysis of (B) BAX, (C) RIPK1, and (D) GPX4 mRNA expression in MCF7, HCT116, and A549 cells. The internal control was used as β-Actin mRNA. Each bar represents mean ± SD. (*P < 0.05, **P < 0.01, ***P < 0.001) (E) Western blot analysis of β-Actin, BAX, RIPK1, and GPX4 expression in MCF7, HCT116, and A549 cells. Confirmation of inhibition effect of Ferrostatin-1, α-tocopherol (vitamin E), and RSL3 in (F) HFBs as well as (G) MCF7, (H) HCT116, and (I) A549 cell lines. Each cell line was treated with RSL3 in the presence or absence of ferostatin-1 and vitamin E, and cell viability was confirmed. Each was performed with three independent samples and values were represented as mean ± SD.

absence of the ferroptosis inhibitor Ferrostatin-1 or vitamin E. Ferrostatin-1 and vitamin E, which are ferroptosis inhibitors, inhibited cell death by FHA NPs and RSL3, which in turn prevented lipid peroxidation, which means that ferroptosis cell death was inhibited. Based on these data, we confirmed that ferroptotic cell death occurred by FHA NPs. Moreover, compared to the results in HFB cells, we confirmed that the tendency of cell death in MCF7, HCT116, and A549 cells was markedly different. The degree of viability was different in each cell line based on the different biological properties of each cell, and we believe that further studies on ferroptosis in several types of cancer will be needed in the future.

In addition, we verified the ROS generation and Lipid peroxidation (LPO) level in the presence or absence of Ferrostatin-1(Fer-1), a ferroptosis inhibitor, after treating the cells with FHA NPs. We conducted qualitative evaluation through fluorescence microscopy and quantitative evaluation through FACS. Each MCF7, HCT116, and A549 cells were treated with 200 μg/mL FHA NPs with or without 4 μg/mL Fer-1 for 12 h, CellROX Orange to check ROS, BODIPY 581/591C11 to check LPO generation was used to confirm. As shown in Fig. 6A and C, S18, S19, S20, S21, S22, S23, when only FHA NPs were treated, we confirmed that ROS was generated and a fairly high level of lipid peroxidation occurred. In addition, the generation of ROS or LPO level was significantly reduced in the Fer-1 treatment group compared to the case where only FHA nanoparticles were treated, and similar results were confirmed in FACS evaluation Fig. 6B and D.

In general, the change in the morphology and function of mitochondria is a process that occurs through ferroptosis, and we were confirmed using MitoTracker to identify the relevance of FHA NPs. After treating A549 cells with FHA NPs for 12 h, the fluorescence intensity was investigated through MitoTraker. And we confirmed that the fluorescence intensity of mitochondria increased, and numerous fragmented sort-tubular mitochondria were observed compared to the control group (Fig. 6E). When most nanoparticles are exposed to cells, they converge into lysosomes and degrade again, and cellular internalization is an important part of nanoparticle delivery. We confirmed using LysoTraker to observe changes in intracellular particle pathways and organelles after treatment with FHA NPs. After treating A549 cells with FHA NPs for 12 h, we examined the fluorescence intensity through LysoTraker, we confirmed the abnormal fluorescence intensity elevations of the lysosome than the Control group(Ctrl). A significant increase in the fluorescence signal indicates autophagic activation, and we confirmed the correlation between FHA NPs and lysosomes (Fig. 6F). Then, using FerroOrange, the intracellular location of Fe^{2+} that can be confirmed in living cells was confirmed. After treating A549 cells with FHA NPs for 24 h, we examined the fluorescence intensity through FerroOrange and LysoTraker. When compared with the group(Ctrl) not treated with FHA NPs, both FerroOrange and LysoTraker fluorescence intensity increased, and colocalization was confirmed, confirming that a large amount of iron in the FHA NPs was present in the lysosome (Fig. 6G).

3.5. *Evaluation of therapeutic effects of FHA NPs activating ferroptosis in vivo*

To evaluate the ferroptotic tumor suppression of FHA NPs *in vivo*, A549 cells were used to establish subcutaneous tumors in nude mice. Tumors were allowed to grow until an average initial tumor volume of 330 mm^3 was achieved, and mice were randomly divided into groups of 0, 12, and 24 h as well as 3, 7, 14, and 21 days. Using a multiple-dose delivery scheme, 8 mg/kg FHA NPs or phosphate-buffered saline (PBS) was injected at a peritumoral site every 24 h in immunosuppressed mice (n = 3) bearing A549 tumors for 21 days (Fig. 7A).

Fig. S24 shows the profiled daily weight change, demonstrating that the bodyweight of the FHA NP-treated group was decreased compared to the PBS group (control). We confirmed that the size of the tumor of the FHA NPs-treated group was significantly reduced than the control group. In the FHA NP treatment group, the initial tumor volume of 330 mm^3 was

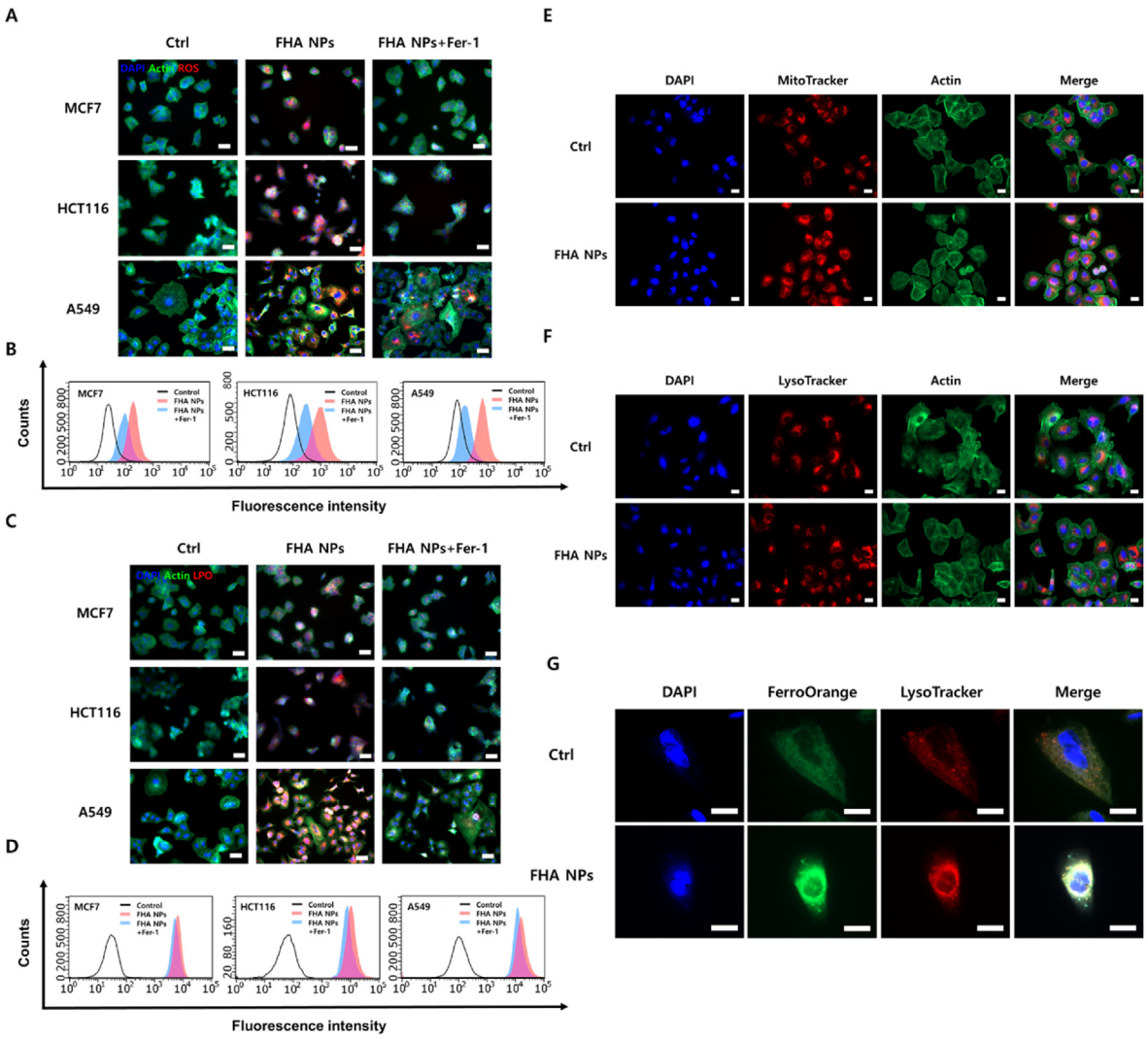

Fig. 6. Confirmation of ROS and Lipid peroxidation (LPO) expression levels according to the presence of Ferrostatin-1 and lysosome and mitochondrial changes after treated FHA NPs. (A) Fluorescence images to confirm ROS generation in the presence or absence of Ferrostatin-1(Fer-1) under exposure to FHA NPs in MCF7, HCT116, and A549 cells. (scale bar: 50 μm) (B) FACS analysis to confirm ROS generation in the presence or absence of Fer-1 exposed to FHA NPs in MCF7, HCT116, and A549 cells. (C) Fluorescence images to confirm LPO levels in the presence or absence of Fer-1 under exposure to FHA NPs in MCF7, HCT116, and A549 cells. (scale bar: 50 μm) (D) FACS analysis to confirm LPO levels in the presence or absence of Fer-1 exposed to FHA NPs in MCF7, HCT116, and A549 cells. (E) Fluorescent images of MitoTracker staining to assess the mitochondrial morphology in A549 cells. Blue, red, and green represent nuclear, mitochondria, and actin filaments, respectively. (scale bar: 20 μm) (F) Fluorescent images of MitoTracker staining in A549 cells. Blue, red, and green represent nuclear, lysosome, and actin filaments, respectively. (scale bar: 20 μm) (G) FerroOrange and LysoTracker staining in A549 cells. Blue, green, and red represent nuclear, FerroOrange, and lysosome, respectively. (scale bar: 20 μm).

reduced to 32 ± 20 mm^3. Thus, only approximately 10% of the tumor remained. However, in the control group treated with PBS, the tumor grew to 1576 ± 210 mm^3 after 21 days (Fig. 7B and S25). Moreover, the weight of the tumor increased from 0.35 ± 0.04 g to 1.0 ± 0.4 g in the PBS-injected group (Fig. 7C), and the tumor weight decreased from 0.36 ± 0.02 g to 0.03 ± 0.01 g in the FHA NP-injected group (Fig. 7D). After treatment, different groups of tumors were harvested and photographed, and tumors treated with FHA NP were much smaller in both weight and visible size, which was consistent with tumor growth data (Fig. 7E). All of the mice survived the experimental period of 21 days (Fig. S26), and Fig. S27 presents IVIS 200 optical images, revealing changes in mouse tumors in groups treated with FHA NPs or PBS after 21 days, separately.

Fig. 7F shows the distribution of FHA NPs within the tumor, heart, lung, spleen, liver, and kidney using MR imaging. Compared to the lower-left circle, which represents the water signal, the MRI signal of the group injected with PBS or FHA NPs was clearly identified compared with the MRI signal of tumors and other organs. Overall, we confirmed that the synthesized FHA NPs exhibited a high density and strong signal only in the tumor without accumulating in other organs. As shown in Fig. 7G, H&E staining of tumor tissues of the group injected with FHA NPs revealed a high level of tumor damage compared to the group injected with PBS. The enlarged image on the right, as indicated by the arrow, showed that distinct and dense nuclei were uniformly distributed in the tumor injected with PBS. However, in the FHA NP-injected group irregular and fewer nuclei with abnormally clumped chromatin were observed.

In this study, we confirmed the induction of ferroptotic cell death by FHA NPs *in vivo* and the possibility of using this system in various studies. FHA NP was effectively targeted to the tumor site with excellent tumor targeting ability, and through this, excellent anti-tumor effects could be confirmed. Although the stability and valuable effect of FHA NPs inducing ferroptosis were confirmed, we performed peritumoral injection due to concerns about the presence of hyaluronidase in our body and its degradation in the blood, which is considered a limitation of our

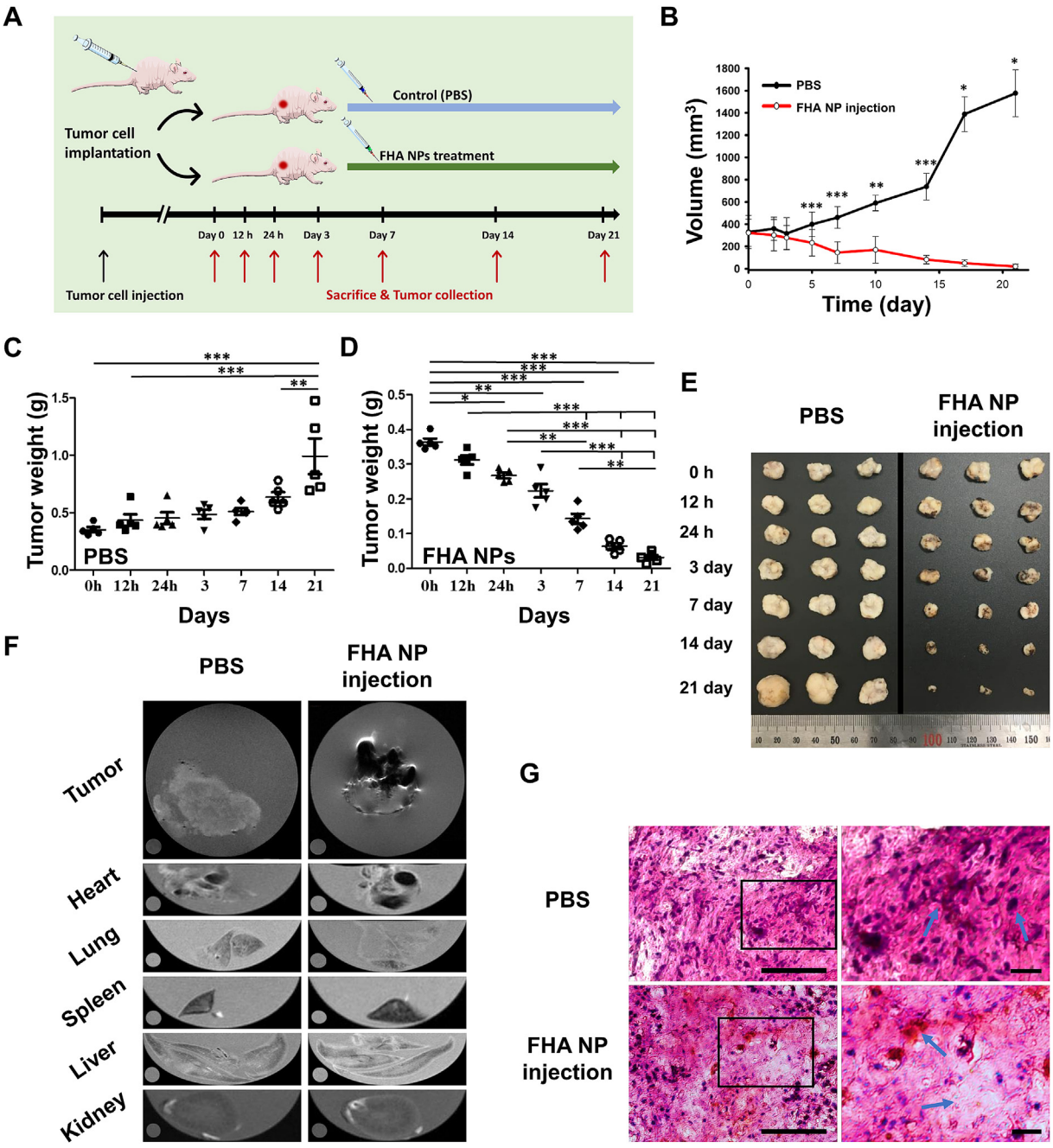

Fig. 7. FHA NP-mediated inhibition of tumor growth and progression *in vivo*. (A) Schematic diagram of the treatment used *in vivo* experiments. (B) The tumor volume differences of A549 tumor-bearing mice administered PBS and FHA NPs for 21 days. Quantitative analysis of tumor weight of (C) PBS groups and (D) FHA NPs groups for 21 days. (E) Photograph of the excised tumor at indicated time points for day 21. (F) MRI imaging in PBS- and FHA NP-injected groups to confirm Fe accumulation in organs and tumors. (G) Histological analysis of tumor sections stained with H & E. (scale bar: 50 μm) *P < 0.05, **P < 0.01, ***P < 0.001.

study. In order to solve this problem, additional research is needed to experimentally verify the targeting, stability, and effectiveness of particles after intravenous injection. Our approach to induce ferroptotic cell death offers promising prospects for the development of nanomedicine in anticancer therapy. For clinical treatment, this type of nanomedicine will greatly enhance the quality of life of the treated subject based on its reduced toxicity and improved anti-tumor effect through ferroptosis. This highly efficient therapeutic nano-platform that induces ferroptosis is expected to provide new insights into the treatment of many types of tumors and exhibit synergistic therapeutic effects with other treatment methods in the future.

4. Conclusions

In summary, the importance of ferroptosis in tumor treatment has been highlighted as a new treatment alternative that can overcome the existing treatment barriers of cancer nanomedicine. In this study, biocompatible HA-based NPs containing Fe ions were engineered to induce iron-dependent ferroptosis. FHA NPs target tumors based on the specific targeting of the HA receptor CD44 and react in cancer cells without affecting normal cells. We demonstrated that FHA NPs induced ROS expression via the Fe reaction and induced ferroptotic cell death at both the cellular and animal levels. We consequently observed a potent

ferroptosis treatment effect in tumor models. This nano-platform that induces ferroptosis was designed safely with actual clinical applications in mind and confirmed the potential for clinical application and expandability. We believe that this study will be a safe way to improve therapeutic effectiveness along with conventional treatments as an effective tool for anticancer therapy.

Credit author statement

Chaewon Bae: Conceptualization, Investigation, Resources Data curation and Visualization, Writing – original draft, Writing-Reviewing, and Editing. Hyerim Kim: Methodology, Investigation, Writing-Reviewing. Yun-Min Kook: Methodology, Investigation, Validation. Chaedong Lee: Validation, Formal analysis. Changheon Kim: Resources Data curation, Visualization. Chungmo Yang: Resources Data curation and Visualization, Writing- Reviewing. Min Hee Park: Methodology, Resources Data curation and Visualization, Writing- Reviewing. Yuanzhe Piao: Validation, Methodology, Writing- Reviewing. Won-Gun Koh: Methodology, Writing-Reviewing. Kangwon Lee: Supervision, Conceptualization, Validation, Writing-Reviewing and Editing, Funding acquisition, Project administration.

Declaration of competing interest

The authors declare that they have no known competing financial interests or personal relationships that could have appeared to influence the work reported in this paper.

Data availability

No data was used for the research described in the article.

Acknowledgements

This work was supported by the Bio & Medical Technology Development Program of the National Research Foundation (NRF) funded by the South Korea Ministry of Science and ICT (grant no. 2016M3A9B4919711) and Nano & Material Technology Development Program through the National Research Foundation (NRF) funded by the South Korea Ministry of Science and ICT (grant no. 2017M3A7B4049850).

Appendix B. Supplementary data

Supplementary data to this article can be found online at https://doi.org/10.1016/j.mtbio.2022.100457.

Appendix A. Supplementary data

The following is the Supplementary data to this article:

References

[1] K. Riehemann, S.W. Schneider, T.A. Luger, B. Godin, M. Ferrari, H. Fuchs, Nanomedicine-challenge and perspectives, Angew. Chem., Int. Ed. 48 (5) (2009) 872–897.
[2] A. Shapira, Y.D. Livney, H.J. Broxterman, Y.G. Assaraf, Nanomedicine for targeted cancer therapy: towards the overcoming of drug resistance, Drug Resist. Updates 14 (3) (2011) 150–163.
[3] A. Wicki, D. Witzigmann, V. Balasubramanian, J. Huwyler, Nanomedicine in cancer therapy: challenges, opportunities, and clinical applications, J. Contr. Release 200 (2015) 138–157.
[4] J.J. Shi, P.W. Kantoff, R. Wooster, O.C. Farokhzad, Cancer nanomedicine: progress, challenges and opportunities, Nat. Rev. Cancer 17 (1) (2017) 20–37.
[5] D.E. Owens, N.A. Peppas, Opsonization, biodistribution, and pharmacokinetics of polymeric nanoparticles, Int. J. Pharm. 307 (1) (2006) 93–102.
[6] J.A. Champion, Y.K. Katare, S. Mitragotri, Particle shape: a new design parameter for micro- and nanoscale drug delivery carriers, J. Contr. Release 121 (1–2) (2007) 3–9.
[7] B. Sumer, J.M. Gao, Theranostic nanomedicine for cancer, Nanomedicine-Uk 3 (2) (2008) 137–140.
[8] A.Z. Wilczewska, K. Niemirowicz, K.H. Markiewicz, H. Car, Nanoparticles as drug delivery systems, Pharmacol. Rep. 64 (5) (2012) 1020–1037.
[9] S.D. Steichen, M. Caldorera-Moore, N.A. Peppas, A review of current nanoparticle and targeting moieties for the delivery of cancer therapeutics, Eur. J. Pharmaceut. Sci. 48 (3) (2013) 416–427.
[10] M.K. Yu, J. Park, S. Jon, Targeting strategies for multifunctional nanoparticles in cancer imaging and therapy, Theranostics 2 (1) (2012) 3–44.
[11] S. Fulda, K.M. Debatin, Extrinsic versus intrinsic apoptosis pathways in anticancer chemotherapy, Oncogene 25 (34) (2006) 4798–4811.
[12] R.J. Bold, P.M. Termuhlen, D.J. McConkey, Apoptosis, cancer and cancer therapy, Surg Oncol 6 (3) (1997) 133–142.
[13] R.S. Sidhu, A.P. Bollon, Tumor-necrosis-factor Activities and cancer-therapy - a perspective, Pharmacol. Therapeut. 57 (1) (1993) 79–128.
[14] M.V. Jain, A.M. Paczulla, T. Klonisch, F.N. Dimgba, S.B. Rao, K. Roberg, F. Schweizer, C. Lengerke, P. Davoodpour, V.R. Palicharla, S. Maddika, M. Los, Interconnections between apoptotic, autophagic and necrotic pathways: implications for cancer therapy development, J. Cell Mol. Med. 17 (1) (2013) 12–29.
[15] Z. Su, Z. Yang, L. Xie, J.P. DeWitt, Y. Chen, Cancer therapy in the necroptosis era, Cell Death Differ. 23 (5) (2016) 748–756.
[16] S.J. Dixon, K.M. Lemberg, M.R. Lamprecht, R. Skouta, E.M. Zaitsev, C.E. Gleason, D.N. Patel, A.J. Bauer, A.M. Cantley, W.S. Yang, B. Morrison, B.R. Stockwell, Ferroptosis: an iron-dependent form of nonapoptotic cell death, Cell 149 (5) (2012) 1060–1072.
[17] A.R. Bogdan, M. Miyazawa, K. Hashimoto, Y. Tsuji, Regulators of iron homeostasis: new players in metabolism, cell death, and disease, Trends Biochem. Sci. 41 (3) (2016) 274–286.
[18] H.T. Yu, P.Y. Guo, X.Z. Xie, Y. Wang, G. Chen, Ferroptosis, a new form of cell death, and its relationships with tumourous diseases, J. Cell Mol. Med. 21 (4) (2017) 648–657.
[19] Y. Xie, W. Hou, X. Song, Y. Yu, J. Huang, X. Sun, R. Kang, D. Tang, Ferroptosis: process and function, Cell Death Differ. 23 (3) (2016) 369–379.
[20] S.E. Kim, L. Zhang, K. Ma, M. Riegman, F. Chen, I. Ingold, M. Conrad, M.Z. Turker, M.H. Gao, X.J. Jiang, S. Monette, M. Pauliah, M. Gonen, P. Zanzonico, T. Quinn, U. Wiesner, M.S. Bradbury, M. Overholtzer, Ultrasmall nanoparticles induce ferroptosis in nutrient-deprived cancer cells and suppress tumour growth, Nat. Nanotechnol. 11 (11) (2016) 977–985.
[21] D.W. Zheng, Q. Lei, J.Y. Zhu, J.X. Fan, C.X. Li, C. Li, Z.S. Xu, S.X. Cheng, X.Z. Zhang, Switching apoptosis to ferroptosis: metal-organic network for high-efficiency anticancer therapy, Nano Lett. 17 (1) (2017) 284–291.
[22] S.F. Wang, F.Y. Li, R.R. Qiao, X. Hu, H.R. Liao, L.M. Chen, J.H. Wu, H.B. Wu, M. Zhao, J.N. Liu, R. Chen, X.B. Ma, D. Kim, J.H. Sun, T.P. Davis, C.Y. Chen, J. Tian, T. Hyeon, D. Ling, Arginine-rich manganese silicate nanobubbles as a ferroptosis-inducing agent for tumor-targeted theranostics, ACS Nano 12 (12) (2018) 12380–12392.
[23] F. Zhang, F. Li, G.H. Lu, W.D. Nie, L.J. Zhang, Y.L. Lv, W.E. Bao, X.Y. Gao, W. Wei, K.Y. Pu, H.Y. Xie, Engineering magnetosomes for ferroptosis/immunomodulation synergism in cancer, ACS Nano 13 (5) (2019) 5662–5673.
[24] X. Meng, J. Deng, F. Liu, T. Guo, M.Y. Liu, P.P. Dai, A.P. Fan, Z. Wang, Y.J. Zhao, Triggered all-active metal organic framework: ferroptosis machinery contributes to the apoptotic photodynamic antitumor therapy, Nano Lett. 19 (11) (2019) 7866–7876.
[25] T. Liu, W.L. Liu, M.K. Zhang, W.Y. Yu, F. Gao, C.X. Li, S.B. Wang, J. Feng, X.Z. Zhang, Ferrous-supply-regeneration nanoengineering for cancer-cell-specific ferroptosis in combination with imaging-guided photodynamic therapy, ACS Nano 12 (12) (2018) 12181–12192.
[26] M.Z. Zhang, X.H. Qin, Z.P. Zhao, Q. Du, Q. Li, Y. Jiang, Y.X. Luan, A self-amplifying nanodrug to manipulate the Janus-faced nature of ferroptosis for tumor therapy, Nanoscale Horiz 7 (2) (2022) 198–210.
[27] R.D. Song, T.L. Li, J.Y. Ye, Sun F, B. Hou, M. Saeed, J. Gao, Y.J. Wang, Q.W. Zhu, Z. Xu, H.J. Yu, Acidity-Activatable Dynamic Nanoparticles Boosting Ferroptotic Cell Death for Immunotherapy of Cancer, Adv Mater 33 (31) (2021).
[28] K. Kim, H. Choi, E.S. Choi, M.H. Park, J.H. Ryu, Hyaluronic acid-coated nanomedicine for targeted cancer therapy, Pharmaceutics 11 (7) (2019).
[29] S.Y. Lee, M.S. Kang, W.Y. Jeong, D.W. Han, K.S. Kim, Hyaluronic acid-based theranostic nanomedicines for targeted cancer therapy, Cancers 12 (4) (2020).
[30] P.J. Flory, Molecular size distribution in three dimensional polymers. II. Trifunctional branching units, J. Am. Chem. Soc. 63 (1941) 3091–3096.
[31] K. Vorvolakos, I.S. Isayeva, H.M. Luu, D.V. Patwardhan, S.K. Pollack, Ionically cross-linked hyaluronic acid: wetting, lubrication, and viscoelasticity of a modified adhesion barrier gel, Med Devices (Auckl) 4 (2011) 1–10.
[32] R.J. Peach, D. Hollenbaugh, I. Stamenkovic, A. Aruffo, Identification of hyaluronic-acid binding-sites in the extracellular domain of Cd44, J. Cell Biol. 122 (1) (1993) 257–264.
[33] J. Lesley, Q. He, K. Miyake, A. Hamann, R. Hyman, P.W. Kincade, Requirements for hyaluronic-acid binding by Cd44 - a role for the cytoplasmic domain and activation by antibody, J. Exp. Med. 175 (1) (1992) 257–266.
[34] M. Zoller, CD44: can a cancer-initiating cell profit from an abundantly expressed molecule? Nat. Rev. Cancer 11 (4) (2011) 254–267.
[35] W.T. Winter, S. Arnott, Hyaluronic acid: the role of divalent cations in conformation and packing, J. Mol. Biol. 117 (3) (1977) 761–784.
[36] L. Jiang, N. Kon, T.Y. Li, S.J. Wang, T. Su, H. Hibshoosh, R. Baer, W. Gu, Ferroptosis as a p53-mediated activity during tumour suppression, Nature 520 (7545) (2015) 57–+.

[37] M.H. Gao, P. Monian, Q.H. Pan, W. Zhang, J. Xiang, X.J. Jiang, Ferroptosis is an autophagic cell death process, Cell Res. 26 (9) (2016) 1021–1032.
[38] Z.Y. Shen, T. Liu, Y. Li, J. Lau, Z. Yang, W.P. Fan, Z.J. Zhou, C.R. Shi, C.M. Ke, V.I. Bregadze, S.K. Mandal, Y.J. Liu, Z.H. Li, T. Xue, G.Z. Zhu, J. Munasinghe, G. Niu, A.G. Wu, X.Y. Chen, Fenton-reaction-acceleratable magnetic nanoparticles for ferroptosis therapy of orthotopic brain tumors, ACS Nano 12 (11) (2018) 11355–11365.
[39] Y.J. He, X.Y. Liu, L. Xing, X. Wan, X. Chang, H.L. Jiang, Fenton reaction-independent ferroptosis therapy via glutathione and iron redox couple sequentially triggered lipid peroxide generator, Biomaterials (2020) 241.
[40] Z.Y. Shen, J.B. Song, B.C. Yung, Z.J. Zhou, A.G. Wu, X.Y. Chen, Emerging strategies of cancer therapy based on ferroptosis, Adv. Mater. 30 (12) (2018).
[41] S. Boutry, D. Forge, C. Burtea, I. Mahieu, O. Murariu, S. Laurent, L.V. Elst, R.N. Muller, How to quantify iron in an aqueous or biological matrix: a technical note, Contrast Media Mol. Imaging 4 (6) (2009) 299–304.
[42] X.M. Zhu, Y.X.J. Wang, K.C.F. Leung, S.F. Lee, F. Zhao, D.W. Wang, J.M.Y. Lai, C. Wan, C.H.K. Cheng, A.T. Ahuja, Enhanced cellular uptake of aminosilane-coated superparamagnetic iron oxide nanoparticles in mammalian cell lines, Int. J. Nanomed. 7 (2012) 953–964.
[43] S.V. Torti, F.M. Torti, Iron and cancer: more ore to be mined, Nat. Rev. Cancer 13 (5) (2013) 342–355.
[44] W.S. Yang, R. SriRamaratnam, M.E. Welsch, K. Shimada, R. Skouta, V.S. Viswanathan, J.H. Cheah, P.A. Clemons, A.F. Shamji, C.B. Clish, L.M. Brown, A.W. Girotti, V.W. Cornish, S.L. Schreiber, B.R. Stockwell, Regulation of ferroptotic cancer cell death by GPX4, Cell 156 (1–2) (2014) 317–331.
[45] J.P.F. Angeli, M. Schneider, B. Proneth, Y.Y. Tyurina, V.A. Tyurin, V.J. Hammond, N. Herbach, M. Aichler, A. Walch, E. Eggenhofer, D. Basavarajappa, O. Radmark, S. Kobayashi, T. Seibt, H. Beck, F. Neff, I. Esposito, R. Wanke, H. Forster, O. Yefremova, M. Heinrichmeyer, G.W. Bornkamm, E.K. Geissler, S.B. Thomas, B.R. Stockwell, V.B. O'Donnell, V.E. Kagan, J.A. Schick, M. Conrad, Inactivation of the ferroptosis regulator Gpx4 triggers acute renal failure in mice, Nat. Cell Biol. 16 (12) (2014), 1180-U120.
[46] W.X. Zong, C. Li, G. Hatzivassiliou, T. Lindsten, Q.C. Yu, J.Y. Yuan, C.B. Thompson, Bax and Bak can localize to the endoplasmic reticulum to initiate apoptosis, J. Cell Biol. 162 (1) (2003) 59–69.
[47] D.M. Moujalled, W.D. Cook, T. Okamoto, J. Murphy, K.E. Lawlor, J.E. Vince, D.L. Vaux, TNF can activate RIPK3 and cause programmed necrosis in the absence of RIPK1, Cell Death Dis. 4 (2013).
[48] X.B. Sui, R.N. Zhang, S.P. Liu, T. Duan, L.J. Zhai, M.M. Zhang, X.M. Han, Y. Xiang, X.X. Huang, H.M. Lin, T. Xie, RSL3 drives ferroptosis through GPX4 inactivation and ROS production in colorectal cancer, Front. Pharmacol. 9 (2018).